J Supercond Nov Magn (2015) 28:2539–2552
DOI 10.1007/s10948-015-3054-1

ORIGINAL PAPER

A Novel Synthesis of Zn^{2+}-Doped $CoFe_2O_4$ Spinel Nanoparticles: Structural, Morphological, Opto-magnetic and Catalytic Properties

E. Hema[1] · A. Manikandan[2] · P. Karthika[1] · S. Arul Antony[2] · B. R. Venkatraman[3]

Received: 12 February 2015 / Accepted: 27 March 2015 / Published online: 24 April 2015

Abstract Zn^{2+}-doped $CoFe_2O_4$ ($Zn_xCo_{1-x}Fe_2O_4$: where $x = 0.0$, 0.2, 0.4, 0.6, 0.8, and 1.0) spinel nanoparticles (NPs) were synthesized by microwave combustion method using nitrates of cobalt, zinc, and iron as the starting materials and urea used as the fuel. Powder X-ray diffraction (XRD), Fourier transform infrared (FT-IR), energy dispersive X-ray (EDX), and selected area electron diffraction (SAED) pattern analyses showed that all composition was found to have pure cubic spinel structure with well crystalline nature. The average crystallite size of the samples was found to be in the range of 25.43 and 29.46 nm. The lattice parameter increased from 8.432 to 8.441 Å with increasing the Zn^{2+} content, due to the smaller ionic radius of Co^{2+} substituted by larger ionic radius of Zn^{2+}, which was determined by Rietveld analysis. High-resolution scanning electron microscopy (HR-SEM) and transmission electron microscopy (HR-TEM) analyses were used to study the morphological variation, and the results showed a nano-sized spherical-shaped particle-like morphology. The band gap (E_g) of the undoped $CoFe_2O_4$ was estimated to be 2.69 eV from UV-Vis diffuse reflectance spectroscopy (DRS). With the increase of Zn^{2+} dopant, the E_g value decreased from 2.61 to 2.01 eV, due to the difference of particle size of the samples. The magnetic hysteresis ($M - H$) loop confirmed the ferromagnetic nature of undoped $CoFe_2O_4$ with magnetization (M_s) of 64.85 emu/g, and it is decreased with increasing the Zn^{2+} content in $CoFe_2O_4$ spinel, which was confirmed by a vibrating sample magnetometer (VSM). All composition of spinel $Zn_xCo_{1-x}Fe_2O_4$ samples were successfully tested as catalyst for the conversion of benzyl alcohol, which has resulted 91.73 and 95.82 % conversion efficiency of $CoFe_2O_4$ and $Zn_{0.4}Co_{0.6}Fe_2O_4$ nano-catalysts, respectively.

Keywords Spinel ferrites · Nano-catalysts · X-ray diffraction · Electron microscopy · Optical properties · Magnetic properties

✉ E. Hema
hema_chithra@yahoo.in

✉ A. Manikandan
mkavath15@gmail.com

[1] Department of Chemistry, Kunthavai Naacchiyaar Government Arts College for Women (Autonomous), Thanjavur - 613007, Tamil Nadu, India

[2] PG and Research Department of Chemistry, Presidency College (Autonomous), Chennai - 600005, Tamil Nadu, India

[3] PG and Research Department of Chemistry, Periyar E.V.R. College (Autonomous), Tiruchirappalli - 620023, Tamil Nadu, India

1 Introduction

Recently, magnetic nanoparticles (NPs) have been widely investigated by many researchers, due to their excellent unique properties than those of their same bulk materials [1–5]. Magnetic spinel ferrites with a general formula $M^{2+}(Fe^{3+})_2O_4$ ($M^{2+} = Ni^{2+}$, Co^{2+}, Cu^{2+}, Mn^{2+}, etc.) have been most exciting materials, where M^{2+} and Fe^{3+} ions can occupy either tetrahedral (A-) or octahedral (B-) sites and oxygen has a face-centered cubic (*fcc*) close packing arrangement [6–10]. Among them, cobalt ferrite, $CoFe_2O_4$ NPs are an important magnetic material

and gaining much interest in the area of catalysis magnetic storage devices, mechanical hardness, chemical stability, microwave and electronic devices, magneto-optical recording, high-density magnetic recording devices, photocatalysis, hydrogen production, and supercapacitors, due to their high coercivity, high chemical stability, and moderate magnetization (M_s = 80 emu/g) at room temperature [6–19].

Many synthesis strategies including hydrothermal, solvothermal, microemulsion, thermal decomposition, sol-gel, combustion, coprecipitation, ball milling, and laser deposition methods are reported for the synthesis of spinel $CoFe_2O_4$ nanostructures [20–30]. The above said methods have some disadvantages, such as their too long time duration, they are energy consuming, and they need very high temperature calcination step, and hence, further development of these methods are restricted to a certain extent. Among the above various methods, microwave combustion technique is one of the most effective, simple, and feasible method for the rapid synthesis with high purity, homogeneity, and improved characteristics of the nanomaterials. The method of microwave combustion route has gained much attention in recent years, due to their products that are pure, ultrafine, and relatively strain free with narrow size distribution. In this method, the microwave energy is transformed into heat energy by strong intermolecular friction and rises the temperature of the precursor materials suddenly [18, 19]. Also, this method offers many advantages over the other said methods, such as simplicity, high crystallinity, and its adequacy for the preparation of large quantities of products without the need of higher processing temperature for calcinations. Generally, metal precursors and fuels are an appropriate stoichiometric ratio controls for the combustion process in accordance with the principle of propellant chemistry. As a result, the morphology, surface area, crystallite size, textural, and other physicochemical properties are largely changed. Also, the use of microwave energy as heating source speeds up the chemical reaction and kinetics, reduces energy loss, and improves economical viability.

The catalytic property of the spinel ferrite nanomaterials crucially depends on the distribution of cations among the A- and B- sites of the spinel lattice. Ramankutty and Sugunan [13] reported spinel $NiFe_2O_4$, $CoFe_2O_4$, and $CuFe_2O_4$ nanostructures by coprecipitation route, and the result of spinel $CoFe_2O_4$ NPs is the most active catalyst at lower activation temperature, while the $CuFe_2O_4$ is the most active one at higher activation temperature and $NiFe_2O_4$ is the least active. Yan et al. [14] have prepared spinel $CuFe_2O_4$, $NiFe_2O_4$, $CoFe_2O_4$, and $ZnFe_2O_4$ nanostructures by a sol-gel method using ethylenediaminetetraacetic acid (EDTA) as a templating agent. The best performance was reported by using spinel $CoFe_2O_4$, whereby the oxidation of benzyl alcohol (63 % yields) with 93 % selectivity in respect of benzaldehyde was achieved. Substitution of magnetic (Mn^{2+}, Ni^{2+}, etc.) and non-magnetic (Zn^{2+}, Cd^{2+}, etc.) cations in spinel ferrites changes their optical, magnetic, and catalytic properties [31], due to the distribution of the cations in between the available A- and B- sites [32]. Several cations have been used as substituent by many researchers [31–33], in order to improve their optical, magnetic, and catalytic properties. However, the detailed study on the optical and catalytic properties of Zn^{2+}-doped $CoFe_2O_4$ spinel nanoparticles by microwave combustion method has not yet been reported so far.

In this aspect, the present investigation attempts to identify the effects of Zn^{2+} doping on structural, morphological, opto-magnetic, and catalytic properties of spinel $CoFe_2O_4$ NPs by microwave combustion method using urea as the fuel. The as-prepared samples were characterized by powder X-ray diffraction (XRD), Rietveld analysis, Fourier transform infrared (FT-IR), high-resolution scanning electron microscopy (HR-SEM), transmission electron microscopy (HR-TEM), energy dispersive X-ray (EDX) spectroscopy, selected area electron diffraction (SAED) pattern, UV-Visible diffuse reflectance spectra (DRS), photoluminescence (PL) spectra, and vibrating sample magnetometer (VSM) techniques, and the obtained results are discussed herein. The final product formed by the catalytic oxidation of benzyl alcohol into benzaldehyde was characterized by gas chromatography (GC). Catalytic oxidation activity tests were carried out and reported the influence of dopant (Zn^{2+}) on the catalytic activity of spinel $CoFe_2O_4$. The best activity and selectivity towards catalytic oxidation of benzyl alcohol into benzaldehyde were observed.

2 Experimental Part

2.1 Materials and Methods

All the chemicals used in this study were of analytical grade obtained from Merck, India and were used as received without further purification. Cobalt nitrate ($Co(NO_3)_2 \cdot 6H_2O$, 98 %), zinc nitrate ($Zn(NO_3)_2 \cdot 6H_2O$, 98 %), ferric nitrate ($Fe(NO_3)_3 \cdot 9H_2O$, 98 %), and urea ($CO(NH_2)_2$) as the fuel are used for this microwave combustion method. Urea served as a fuel, while the nitrates in the precursors served as the oxidizers. The fuel to oxidizer ratio (F/O) was taken to be as per the concept of propellant chemistry. The samples were prepared with the addition of Zn^{2+} of different molar ratios ($Zn_xCo_{1-x}Fe_2O_4$: x = 0.0, 0.2, 0.4, 0.6, 0.8, and 1.0) to $CoFe_2O_4$. The precursor in a beaker was stirred for about 15 min at room temperature to obtain a clear homogeneous solution, transferred into silica

crucible and placed inside a microwave oven (Samsung, India Limited) for irradiation. The sample was irradiated over the precursor solution for 10 min at 850-W output power and frequency 2.54 GHz. Initially, the precursor mixture boiled and underwent evaporation followed by the decomposition with the evolution of gases. When the solution reached the point of spontaneous combustion, it vaporized and instantly became solid. The obtained solid powders were washed well with ethanol and dried at 70 °C for 1 h. The as-prepared samples ($Zn_xCo_{1-x}Fe_2O_4$: $x = 0.0$, 0.2, 0.4, 0.6, 0.8, and 1.0) were labeled as $CoFe_2O_4$, $Zn_{0.2}Co_{0.8}Fe_2O_4$, $Zn_{0.4}Co_{0.6}Fe_2O_4$, $Zn_{0.6}Co_{0.4}Fe_2O_4$, $Zn_{0.8}Co_{0.2}Fe_2O_4$, and $ZnFe_2O_4$, respectively, and then used for further characterizations. The entire microwave combustion process produces spinel $Zn_xCo_{1-x}Fe_2O_4$ ($x = 0.0$, 0.2, 0.4, 0.6, 0.8 and 1.0) nanopowders in a microwave oven within 10 min of time. The proposed microwave-assisted combustion reaction may be as follows:

$$\mathrm{Co\,(NO_3)_2 \cdot 6H_2O_{(S)} + 2Fe\,(NO_3)_3 \cdot 9H_2O_{(S)} + 6.66CO\,(NH_2)_2\ (S) \rightarrow CoFe_2O_4\ (S) + 37.33H_2O_{(g)} \uparrow + 6.66CO_2\ (g) \uparrow + 10.66N_2\ (g) \uparrow}$$

2.2 Characterization Techniques

Structural characterization of spinel $Zn_xCo_{1-x}Fe_2O_4$ ($x = 0.0$, 0.2, 0.4, 0.6, 0.8, and 1.0) samples were performed using a Rigaku Ultima IV high-resolution XRD with CuKα radiation at $\lambda = 1.5418$ Å. Structural refinements using the Rietveld refinement method were carried out using the PDXL program, and both refined lattice parameter and crystallite size of the obtained ferrites are reported. The surface functional groups were analyzed by Thermo Nicolet FT-IR spectrometer. Morphological studies and energy dispersive X-ray analysis have been performed with a Jeol JSM6360 HR-SEM equipped with EDX for elemental chemical analysis. The transmission electron micrographs were carried out by Philips-TEM (CM20) instrument equipped with a SAED microscope for crystal nature analysis. The surface area was derived from the Bruner Emmet Teller (BET) analysis using liquid nitrogen at 77 K using an automatic adsorption instrument (Quantachrome Corp. Nova-1000 gas sorption analyzer). UV-visible DRS was recorded using Cary100 UV-visible spectrophotometer to estimate their band gap (E_g). The PL properties were recorded using a Varian Cary Eclipse fluorescence spectrophotometer. Magnetic measurements were carried out at room temperature using a PMC MicroMag 3900 model VSM equipped with 1-T magnet.

2.3 Catalytic Test

The catalytic oxidation of benzyl alcohol into benzaldehyde using spinel $Zn_xCo_{1-x}Fe_2O_4$ ($x = 0.0$, 0.2, 0.4, 0.6, 0.8, and 1.0) nano-catalysts was carried out in a batch reactor operated under atmospheric conditions. Along with 0.5 g of nano-sized catalysts, 5 mmol of oxidant (H_2O_2) was added ($CoFe_2O_4$, $Zn_{0.2}Co_{0.8}Fe_2O_4$, $Zn_{0.4}Co_{0.6}Fe_2O_4$, $Zn_{0.6}Co_{0.4}Fe_2O_4$, $Zn_{0.8}Co_{0.2}Fe_2O_4$, and $ZnFe_2O_4$), and the contents were heated at 80 °C in an acetonitrile medium for 5 h in a three-necked round bottom flask equipped with a reflux condenser and thermometer. The oxidized products after the catalytic reaction are collected and studied using an Agilent GC spectrometer. The column used for the study was DB-WAX column (capillary column) of length 30 mm, and helium was used as the carrier gas.

3 Results and Discussion

3.1 Powder XRD Analysis

The structural characterization and phase purity of the samples were confirmed by powder XRD analysis. Figure 1a shows the XRD patterns of spinel $Zn_xCo_{1-x}Fe_2O_4$ samples prepared at various concentrations of Zn^{2+} ions ($x = 0.0$, 0.2, 0.4, 0.6, 0.8, and 1.0) in $CoFe_2O_4$ lattice. The main diffraction peaks (2θ) appear at about 29.66°, 35.73°, 37.08°, 42.54°, 53.07°, 56.55°, 62.03°, 70.56°, 74.08°, and 79.05°, which are attributed to the (220), (311), (222), (400), (422), (511), (440), (620), (533), and (444) planes, respectively, and show the characteristics of a single-phase cubic spinel structure with *Fd3m* space group [29]. All diffraction peaks are in fairly good agreement with those of standard patterns for the fcc structure with the JCPDS card no. 22-1086 for $CoFe_2O_4$ and JCPDS card no. 22-1012 for $ZnFe_2O_4$ [33]. The XRD peaks indicate that a well-defined, pure, single-phase spinel structure developed without any impurity and other phase formation during the microwave combustion method. Figure 1b indicates that the centers of the two most intense peaks (220) and (311) are slightly shifted towards the lower diffracted angles with increasing the concentration of Zn^{2+} dopant, which is attributed to the difference in the ionic radii of Zn^{2+} (0.82 Å) and Co^{2+} (0.72 Å) ions; also, the results confirmed the presence of Zn^{2+} dopant in the spinel $CoFe_2O_4$ matrix. The average crystallite size of the spinel $Zn_xCo_{1-x}Fe_2O_4$ ($x = 0.0$, 0.2, 0.4, 0.6, 0.8, and 1.0) NPs was calculated by using the Debye-Scherrer's formula,

$$L = \frac{0.89\lambda}{\beta\cos\theta} \quad (1)$$

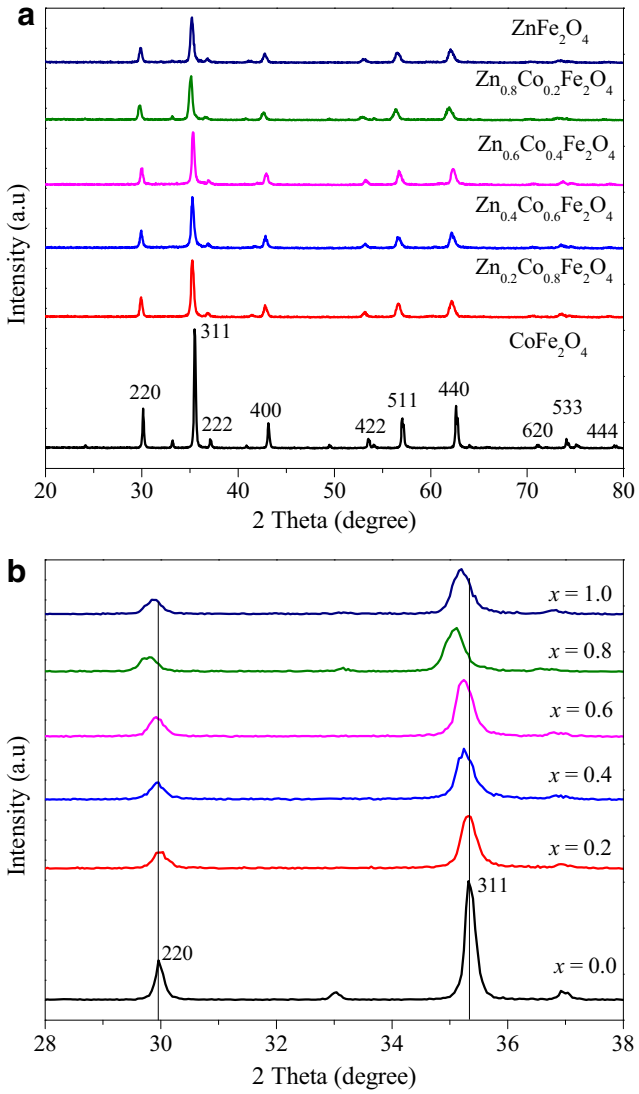

Fig. 1 **a**, **b** Powder XRD patterns of spinel Zn_xCo_{1-x} Fe_2O_4 (x = 0.0, 0.2, 0.4, 0.6, 0.8 and 1.0) NPs

where L is the average crystallite size, λ the X-ray wavelength, θ the Bragg diffraction angle, and β the full width at half maximum (FWHM). The calculated crystallite size of the spinel $Zn_xCo_{1-x}Fe_2O_4$ NPs is summarized in Table 1. The intensity of diffraction peaks decreased significantly with an increase in Zn^{2+} content, which indicates that the increase in the Zn^{2+} doping concentration (x = 0.4) retards the crystallite size. It has been observed that the crystallite size is decreased from 29.46 to 25.43 nm with increase in Zn^{2+} content up to x = 0.0–0.4, and further increase the Zn^{2+} content (x = 0.6–1.0) increased the crystallite size from 26.28 to 27.54 nm. The result reveals that lower concentration of Zn^{2+} dopant (x = 0.0, 0.2, and 0.4) controls and retards the growth of the crystallite size, while higher concentration of Zn^{2+} dopant (x = 0.6, 0.8 and 1.0) favors the growth of the crystallite size at the nucleation centers, which resulted in higher crystallite size. The XRD broadening peaks in spinel $Zn_xCo_{1-x}Fe_2O_4$ NPs strongly suggest that Zn^{2+} ions were successfully substituted into the spinel $CoFe_2O_4$ lattice. However, the undoped $CoFe_2O_4$ sample shows a sharp peak resulting in higher crystallite size. The sample $Zn_{0.4}Co_{0.4}Fe_2O_4$ NPs have a minimum crystallite size of 25.43 nm and show a significant amount of XRD line broadening, a characteristic of nano-sized materials. The calculated crystallite size is in good agreement with the results obtained by Rietveld analysis.

Rietveld analysis is used to characterize the spinel $Zn_xCo_{1-x}Fe_2O_4$ NPs in order to understand their physical properties (lattice parameter and crystallite size). Figure 2 shows the Rietveld refinement XRD pattern of the samples, and the observed values are summarized in Table 1. It was found that the lattice parameter value of undoped $CoFe_2O_4$ is a = 8.432 Å and the value is increased from 8.434 to 8.441 Å with increasing the Zn^{2+} content (x = 0.2 to 1.0). The values of the lattice parameter exhibit an almost linear dependence, thus obeying Vegard's law as shown in Fig. 3. The slight increasing trend in the lattice parameter is due to the replacement of smaller ionic radius of Co^{2+} (0.72 Å) by the larger ionic radius of Zn^{2+} (0.82 Å) [2], in the spinel $CoFe_2O_4$ lattice.

Table 1 Lattice parameter, crystallite size (Scherrer formula, Rietveld analysis) and band gap values of spinel Zn_xCo_{1-x} Fe_2O_4 (x = 0.0, 0.2, 0.4, 0.6, 0.8 and 1.0) NPs

Samples	Lattice parameter (Å)	Crystallite size, L (nm)		Band gap (eV)
	(Rietveld analysis)	Scherrer formula	Rietveld analysis	
$CoFe_2O_4$	8.432	29.46	31	2.69
$Zn_{0.2}Co_{0.8}Fe_2O_4$	8.434	27.84	28	2.61
$Zn_{0.4}Co_{0.6}Fe_2O_4$	8.435	25.43	26	2.54
$Zn_{0.6}Co_{0.4}Fe_2O_4$	8.437	26.28	28	2.51
$Zn_{0.8}Co_{0.2}Fe_2O_4$	8.438	26.96	27	2.50
$ZnFe_2O_4$	8.441	27.54	28	2.01

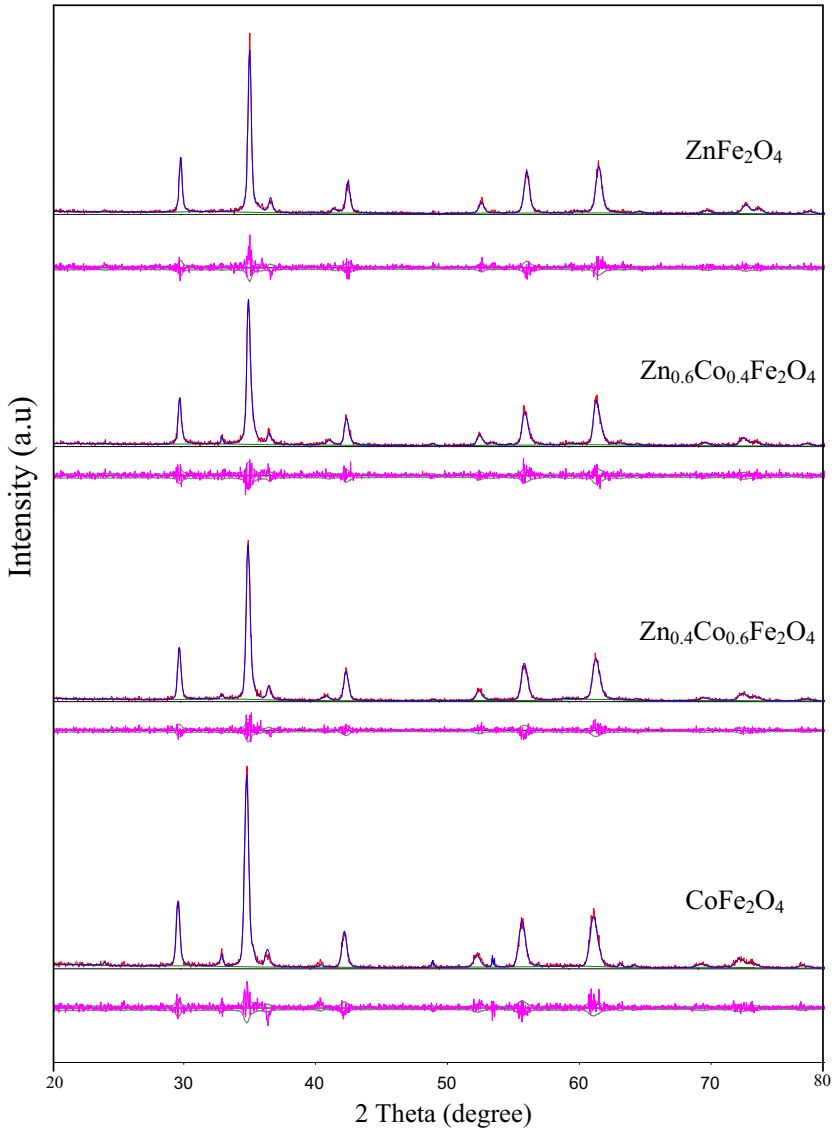

Fig. 2 Rietveld refinement XRD method of spinel $Zn_xCo_{1-x}Fe_2O_4$ ($x = 0.0$, 0.2, 0.4, 0.6, 0.8, and 1.0) NPs

3.2 FT-IR Analysis

Figure 4 shows the FT-IR spectra of spinel $Zn_xCo_{1-x}Fe_2O_4$ ($x = 0.0$, 0.2, 0.4, 0.6, 0.8, and 1.0) NPs. The entire samples exhibit a band around $\sim$ 3400 and 1622 cm^{-1} attributed to the stretching and bending vibrations of O–H groups of water molecule [34, 35]. The characteristic sharp band at around 1320 cm^{-1} corresponds to the $Zn_xCo_{1-x}Fe_2O_4$ system which is due to the out-of-plane bending of O–H stretching, due to adsorbed water molecule [36]. The appearance of bands at about 585 and 458 cm^{-1} is due to the stretching vibrations of B- and A- sites of the spinel $Zn_xCo_{1-x}Fe_2O_4$ system, respectively [35], and confirms the formation of $Zn_xCo_{1-x}Fe_2O_4$ spinel [37].

3.3 HR-SEM Studies

Surface morphologies of the spinel $Zn_xCo_{1-x}Fe_2O_4$ samples were recorded using high-resolution scanning electron microscope (HR-SEM) analysis, and the images are shown in Fig. 5. Figure 5a−d shows the HR-SEM images of spinel $CoFe_2O_4$, $Zn_{0.4}Co_{0.6}Fe_2O_4$, $Zn_{0.6}Co_{0.4}Fe_2O_4$, and $ZnFe_2O_4$ samples, respectively, and indicated that the samples consist of nano-sized spherical-shaped particle-like morphology. The surface morphology shows that all of the particles are well crystallized and admits the agglomerated coalescence behavior of the particles. The observed agglomeration of the nanoparticles may be due to the magnetic interactions among the particles. The crystallite size of the samples obtained from the powder XRD is fairly

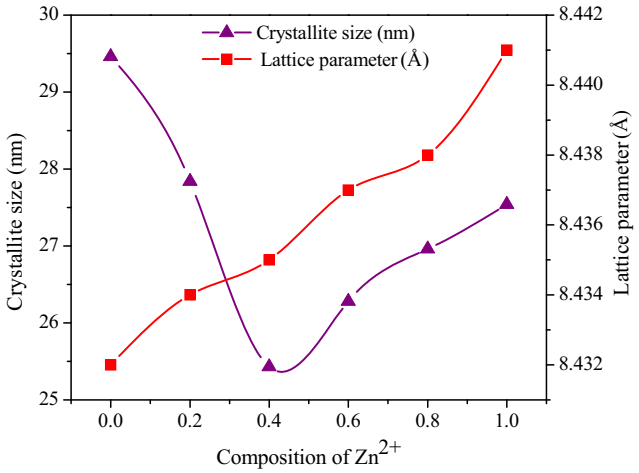

Fig. 3 Evolution of the lattice parameter and crystallite size of spinel $Zn_xCo_{1-x}Fe_2O_4$ ($x = 0.0$, 0.2, 0.4, 0.6, 0.8, and 1.0) NPs

reliable with the particle size determined by HR-SEM. The difference in shape, size, and average grain dimensions is correlated with the crystallite dimensions and ionic radii of the precursors.

3.4 HR-TEM Analysis

To give a further support for the formation of nanoparticle-like morphology and size of the particles, a high-resolution transmission electron microscopy (HR-TEM) analysis was carried out. Figure 6a, b shows the HR-TEM images of spinel $CoFe_2O_4$ and $Zn_{0.4}Co_{0.6}Fe_2O_4$ samples,

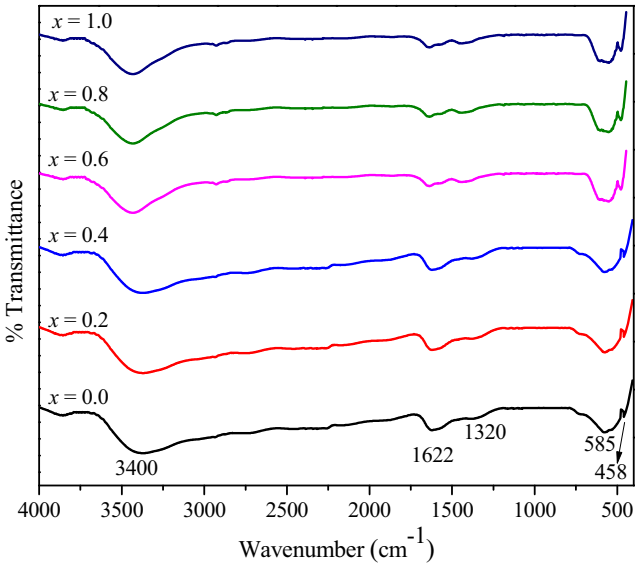

Fig. 4 FT-IR analysis of spinel $Zn_xCo_{1-x}Fe_2O_4$ ($x = 0.0$, 0.2, 0.4, 0.6, 0.8, and 1.0) NPs

respectively. The formation of nanoparticles with uniform size was evident, which is consistent with the average crystallite size obtained from the peak broadening in XRD and Rietveld refinement XRD analysis. The insets of Fig. 6a, b shows the particle distribution diagram of undoped $CoFe_2O_4$ and $Zn_{0.4}Co_{0.6}Fe_2O_4$ samples, respectively. The observed average size of particles of undoped $CoFe_2O_4$ and $Zn_{0.4}Co_{0.6}Fe_2O_4$ samples are 29.46 and 25.43 nm, respectively, which are reliable with the crystallite size of the samples confirmed earlier by XRD and Rietveld refinement XRD analysis.

The nano-sized features are noticeably visible in Fig. 6c, d which were found to be highly crystalline nature. Figure 6c, d shows the inter-planar distance d spacing of 0.242 and 0.236 nm can be assigned to the single phase of spinel $CoFe_2O_4$ and $Zn_{0.4}Co_{0.6}Fe_2O_4$ samples, respectively. The formation of single-phase spinel $Zn_xCo_{1-x}Fe_2O_4$ samples may contain some defects, due to the direct interaction of microwave energy to the raw materials and converted into final products within a few minutes. Figure 6c, d (insets) shows the selected area electron diffraction (SAED) pattern of undoped $CoFe_2O_4$ and $Zn_{0.4}Co_{0.6}Fe_2O_4$ samples, respectively, which implies the single crystalline nature of the products. SAED results show spotty ring characteristic of spinel ferrite nanostructure without any additional diffraction spots, and rings of secondary phases corresponding to the cobalt, zinc, and iron oxides were also observed. From the SAED pattern, there are seven noticeable diffraction rings, the positions of which match well with standard powder diffraction information of spinel $CoFe_2O_4$ and $ZnFe_2O_4$ samples [38].

3.5 EDX Analysis

Energy dispersive X-ray (EDX) analysis of spinel $Zn_xCo_{1-x}Fe_2O_4$ samples are shown in Fig. 7a–d. Figure 7a shows the peaks of Fe, Co, and O elements in undoped $CoFe_2O_4$; Fig. 7b, c shows the peaks of Fe, Zn, Co, and O elements for Zn-doped $CoFe_2O_4$ samples; and Fig. 7d shows the peaks of Fe, Zn, and O elements in $ZnFe_2O_4$ samples, respectively. The percentage of Co–Zn values obtained is given in the insets of Fig. 7a–d. However, the elemental composition of undoped and Zn-doped $CoFe_2O_4$ spinel NPs did not deviate from their initial stoichiometry and matched well with the initial degree of Zn^{2+} substitutions in $CoFe_2O_4$ lattice. In this method, urea was used as the fuel and was interestingly observed to completely favor the formation of spinel $Zn_xCo_{1-x}Fe_2O_4$ samples within few minutes. However, a small peak appeared at 2.1 KeV for all composition, which indicated the presence of Au (gold) peak that has been used as sputter coating, while preparing the sample for HR-SEM analysis for the better visibility of the surface morphology.

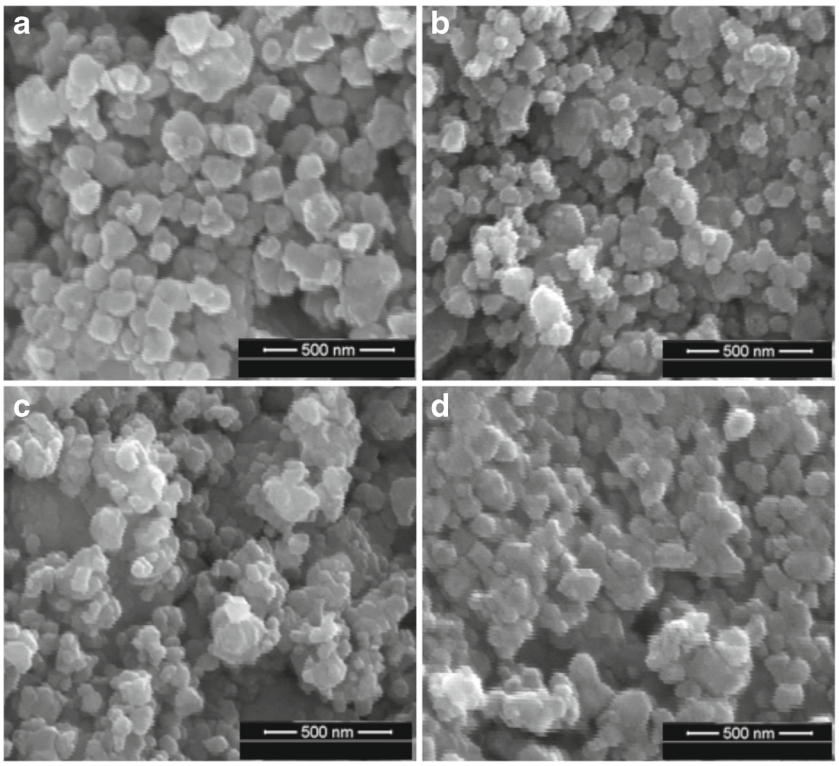

Fig. 5 HR-SEM images of spinel **a** $CoFe_2O_4$, **b** $Zn_{0.4}Co_{0.6}Fe_2O_4$, **c** $Zn_{0.6}Co_{0.4}Fe_2O_4$ and **d** $ZnFe_2O_4$ NPs

3.6 UV-Visible DRS Analysis

To give the significant information in relation to the effect of crystallite size on the band gap energy (E_g) of spinel $Zn_xCo_{1-x}Fe_2O_4$ samples, UV-Visible diffuse reflectance spectroscopy (DRS) analysis was carried out. The E_g of the samples can be evaluated using the Kubelka-Munk method. It allows the calculation of the absorption coefficient (α) by the measurement of UV-Visible diffuse reflectance, and it is mainly used for powder samples. Kubelka-Munk function,

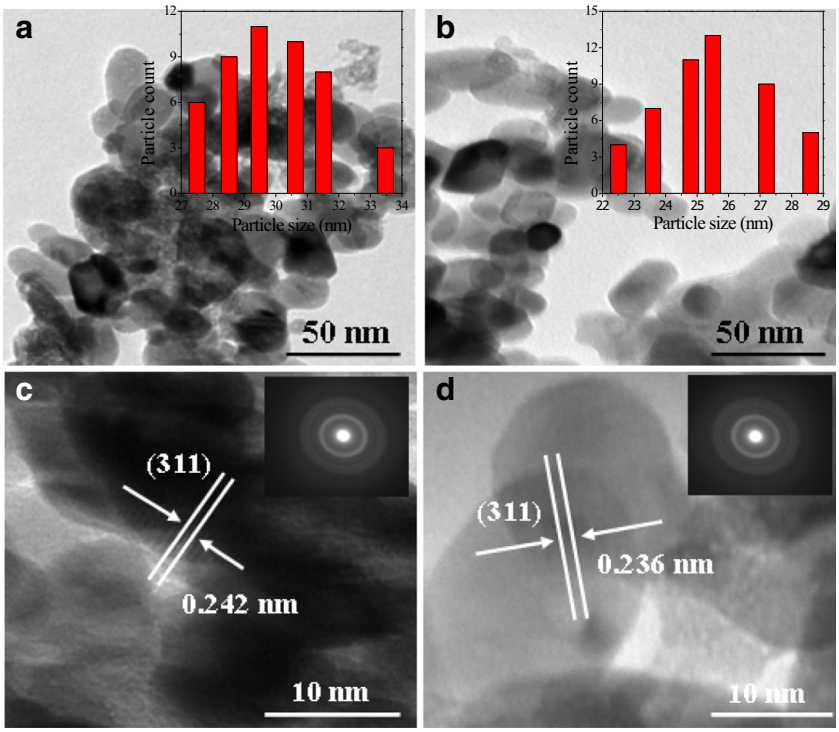

Fig. 6 HR-TEM images of spinel **a**, **c** $CoFe_2O_4$ and **b**, **d** $Zn_{0.4}Co_{0.6}Fe_2O_4$ NPs, insets of Fig. 6a, b the corresponding particle size distribution diagram and Fig. 6c, d (insets), the corresponding SAED patterns of the samples

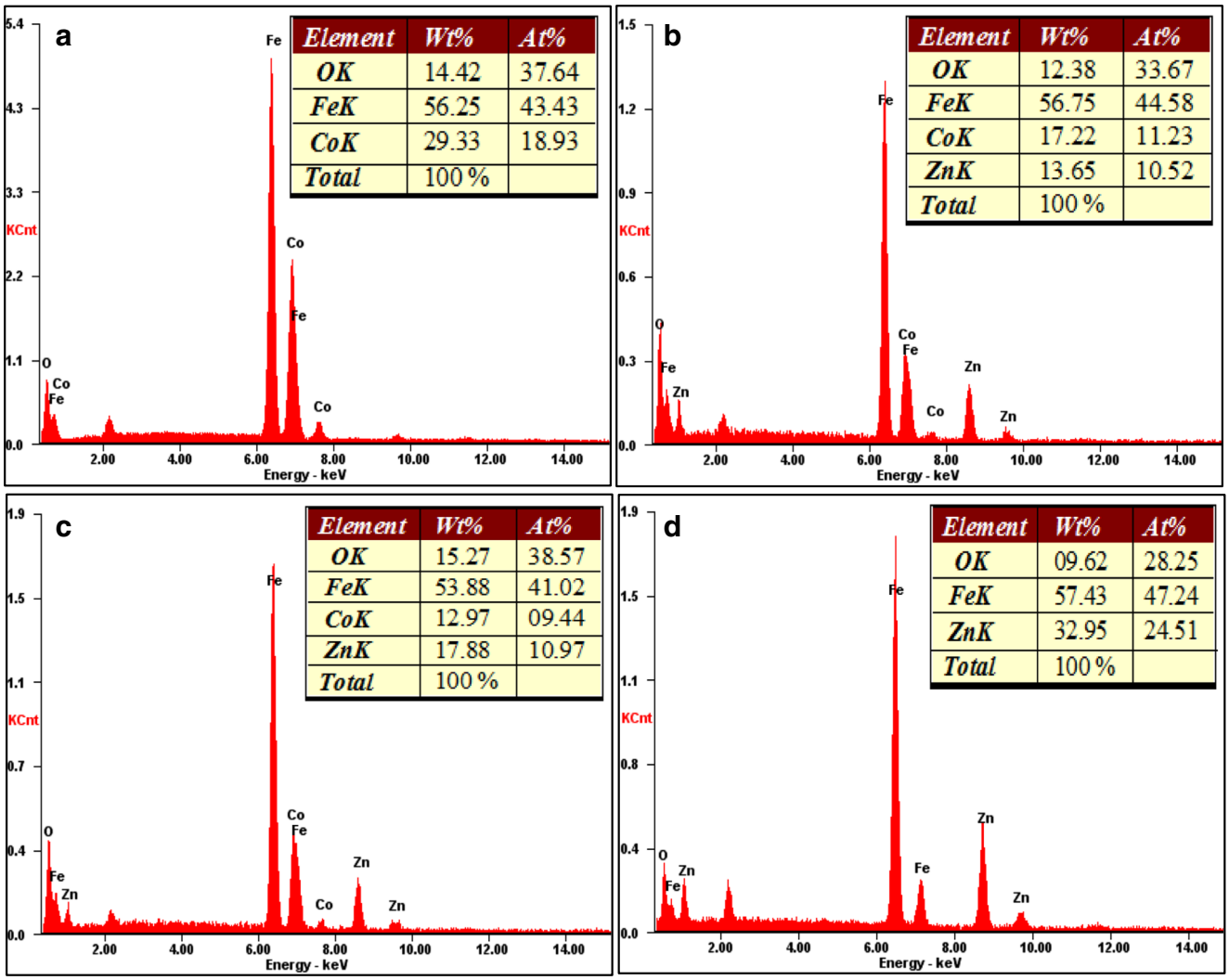

Fig. 7 EDX spectra of spinel **a** $CoFe_2O_4$, **b** $Zn_{0.4}Co_{0.6}Fe_2O_4$, **c** $Zn_{0.6}Co_{0.4}Fe_2O_4$ and **d** $ZnFe_2O_4$ NPs

$F(R)$ is directly proportional to the absorption coefficient (α), and the value is estimated. Thus, the vertical axis is converted into quantity $F(R)$ which is equal to the absorption coefficient. Thus, the α in the Tauc equation is substituted with $F(R)$ and hence the relation becomes,

$$(F(R)) = \alpha = \frac{(1-R)^2}{2R} \tag{2}$$

where, $F(R)$ is the Kubelka-Munk function, α the absorption coefficient, and R the reflectance. Thus the Tauc relation becomes,

$$F(R)h\upsilon = A\left(h\upsilon - E_g\right)^n \tag{3}$$

where $n = 1/2$ and 2 for direct and indirect transitions, respectively, thus giving direct and indirect band gaps. The plots of $(F(R)h\upsilon)^2$ versus $h\upsilon$ for all compositions are shown in Fig. 8. Extrapolation of linear regions of these plots to $(F(R)h\upsilon)^2 = 0$ gives the direct band gap values. The calculated E_g for all compositions are summarized in Table 1. The estimated E_g values of spinel $Zn_xCo_{1-x}Fe_2O_4$ ($x = 0.0$, 0.2, 0.4, 0.6, 0.8, and 1.0) nanoparticles are 2.69, 2.61, 2.54, 2.51, 2.50, and 2.01 eV, respectively (Fig. 9). It is inferred that there is decrease in the E_g of doped samples, when compared to the undoped $CoFe_2O_4$. The E_g value of undoped $CoFe_2O_4$ is 2.69 eV, and hence, there is a red shift for all Zn-doped $CoFe_2O_4$ samples. Chen et al. [29] found a similar value (2.38 eV) for undoped $CoFe_2O_4$ sample. A small decrease in the E_g with decreasing the crystallite size is in contrast to the normal quantum confinement properties [39, 40]. In the present study, the observed direct band gap of undoped $CoFe_2O_4$ and $ZnFe_2O_4$ samples is higher than the bulk materials, which is around 1.95 and 1.9 eV, respectively [41]. The narrowing band gap values with Zn^{2+} dopant in $CoFe_2O_4$ lattice indicates the formation of sub-bands in between the energy band gap and inclusion of their sub-bands with the conduction band (CB) to form a continuous band [42]. However, the optical band gap value

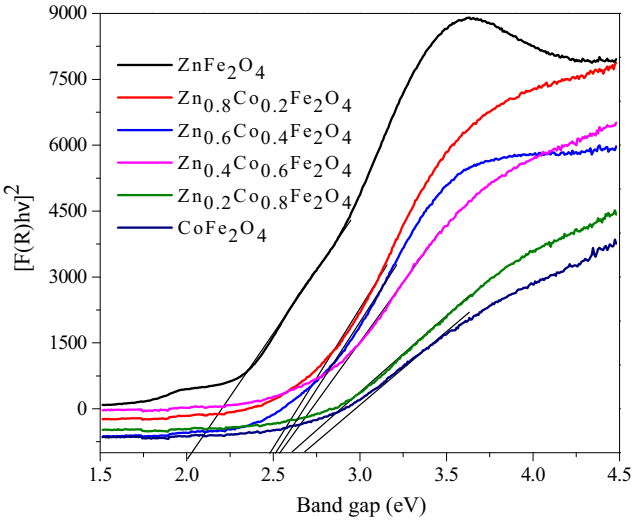

Fig. 8 UV-visible DRS study of spinel Zn_xCo_{1-x} Fe_2O_4(x = 0.0, 0.2, 0.4, 0.6, 0.8, and 1.0) NPs

decreased with the decrease of the particle sizes. This is in contrast to the normal quantum confinement effect. The decrease in band gap energy may also be due to the sp-d exchange interaction between the localized d-electrons of Zn^{2+} ions and band electrons of spinel $CoFe_2O_4$ [43].

3.7 Photoluminescence Spectra

The photoluminescence (PL) spectra were recorded at room temperature to investigate the recombination phenomena and to obtain the information on band gap with the relative energetic position of sub-band gap defect states [44]. However, the nanometer size effect of the particles may reflect in its optical property. Figure 10 shows the room temperature PL spectra of spinel $Zn_xCo_{1-x}Fe_2O_4$ samples recorded at the excitation wavelength of 305 nm for all compositions. In the present study, spinel $Zn_xCo_{1-x}Fe_2O_4$ (x = 0.0, 0.2, 0.4, 0.6, 0.8, and 1.0) samples show peaks corresponding to violet emissions at around 422 and 453 nm. The observed violet emissions may be due to the radiating defects related to the interface traps existing at the grain boundaries [45, 46]. However, a green emission was observed at 531 nm, which may be attributed to the oxygen vacancies [47]. Hence, the emission characteristics in spinel $Zn_xCo_{1-x}Fe_2O_4$ samples formed by the microwave combustion method within a few minutes of time are governed by the defect-controlled processes. Yellow emissions were observed at around 574 and 595 nm, which are attributed to the interstitial oxygen defects. Moreover, two main PL peaks were observed at around 531 and 758 nm, which are usually due to the interstitial defects and oxygen vacancies [48]. Similar results were reported earlier by Chen et al. [29], and they observed two main PL peaks at 520 and 760 nm. However, it was found that the increase of Zn^{2+} ions (x = 0.0–1.0) in $CoFe_2O_4$ matrices increased the PL intensity, due to the increase in distance between the dopant (activator) and the array [49]. The defect centers that act as trap levels and role of Zn^{2+} activators in increasing the PL intensity of the Zn^{2+}-doped $CoFe_2O_4$ play a dominant role in the emission processes.

3.8 VSM Measurements

Magnetic measurements of the samples were carried out at room temperature in order to identify the magnetic behavior of the spinel $Zn_xCo_{1-x}Fe_2O_4$ (x = 0.0, 0.2, 0.4, 0.6, 0.8, and 1.0) samples. The VSM measurements were

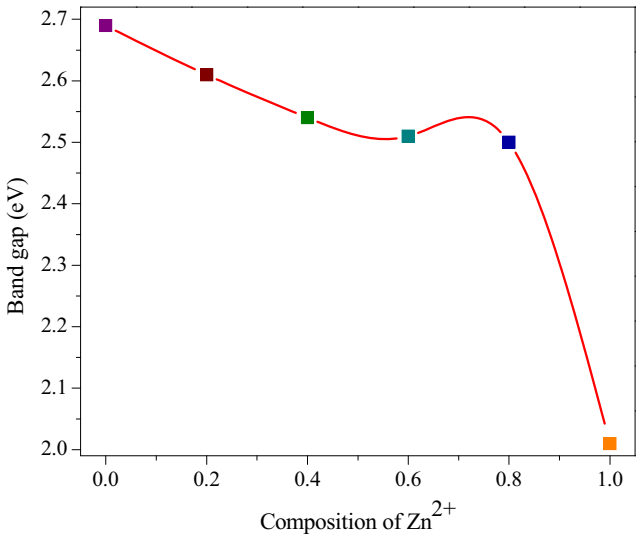

Fig. 9 Variation of the band gap energy of spinel $Zn_xCo_{1-x}Fe_2O_4$ (x = 0.0, 0.2, 0.4, 0.6, 0.8, and 1.0) NPs

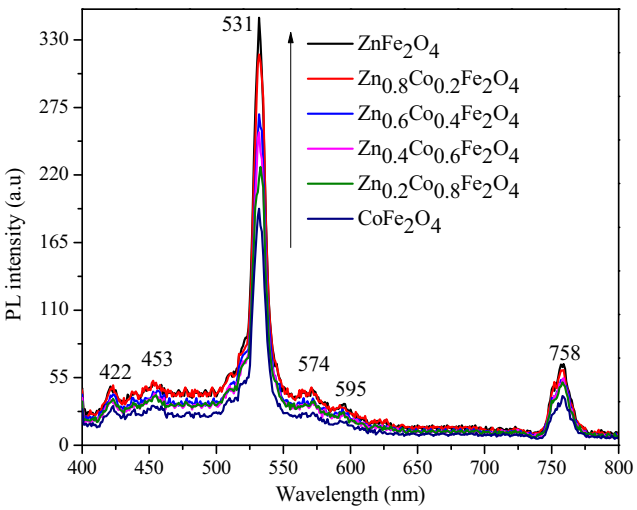

Fig. 10 PL spectra of spinel $Zn_xCo_{1-x}Fe_2O_4$ (x = 0.0, 0.2, 0.4, 0.6, 0.8, and 1.0) NPs

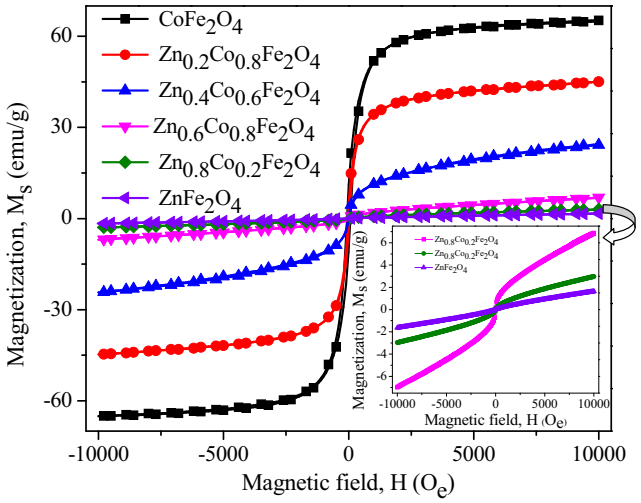

Fig. 11 Magnetic hysteresis (M-H) loops of spinel $Zn_xCo_{1-x}Fe_2O_4$ ($x = 0.0$, 0.2, 0.4, 0.6, 0.8, and 1.0) NPs

recorded in the −10 to +10 kOe applied magnetic field range. The magnetic hysteresis (*M-H*) curve (Fig. 11) confirms that the spinel $Zn_xCo_{1-x}Fe_2O_4$ systems are soft ferrite category. The observed saturation magnetization (M_s), remanent magnetization (M_r), and coercivity (H_c) values are reported in Table 2. Generally, magnetic properties of the spinel ferrites depend on composition as well as cation distribution in between A- and B- site occupancy, and they can exhibit ferromagnetic, anti-ferromagnetic, and paramagnetic nature [50, 51]. The undoped $CoFe_2O_4$ sample shows ferromagnetic behavior, and the magnetization (M_s) increased (64.85 emu/g) with the applied field and does not saturate even at +10 kOe. The prepared lower composition ($x = 0.0$, 0.2, and 0.4) shows a ferromagnetic behavior and the higher compositions ($x = 0.6$, 0.8 and 1.0) show a superparamagnetic behavior (Fig. 11 inset) with hysteresis, and the M_s values decreased with increasing Zn^{2+} content.

The obtained result shows that the value of M_s is higher (64.85 emu/g) for undoped $CoFe_2O_4$, and it is decreased from 45.18 to 2.098 emu/g with increase the concentration of Zn^{2+} ions ($x = 0.2$ to 1.0), which can be attributed to the higher magnetic moments of Co^{2+} ions (3 μB) substituted by the non-magnetic moments of Zn^{2+} (0 μB) ions in spinel $CoFe_2O_4$ lattice [52–54]. A similar trend was reported earlier by Kumar et al. [55], and they observed that the increase of Zn^{2+} content in $CoFe_2O_4$ NPs decreased the M_s values. The decrease in the M_s and H_c values of the samples with an increase in Zn^{2+} dopant in Fig. 12 is due to the lower magneto-crystalline anisotropy of Zn^{2+} with respect to Co^{2+}. The M_s value of undoped $CoFe_2O_4$ (64.85 emu/g) is higher than that of the earlier reported value, i.e., 59.0 emu/g [15], and lower than that of bulk (93.9 emu/g) materials [56]. The observed difference in the value of M_s might be due to particle size, crystalline nature, arrangement of the particles, as well as the nature and composition of the dopant [57, 58]. Similarly, the observed M_s values of the samples are attributed to the lattice defects, magnetic super exchange interaction from the A- to B- sites, and random magnetic orientation of spins on the spinel $Zn_xCo_{1-x}Fe_2O_4$ NPs [59, 60]. However, it was observed that H_c, M_r and M_s values of the spinel $Zn_xCo_{1-x}Fe_2O_4$ ($x = 0.0$, 0.2, 0.4, 0.6, 0.8, and 1.0) NPs gradually decreased with the increase of Zn^{2+} content (Table 2), which can be attributed to the magnetic character and the anisotropic nature of spinel Co–Zn ferrites.

Table 2 Variation of coercivity (H_c), remanant magnetization (M_r) and saturation magnetization (M_s) of spinel $Zn_xCo_{1-x}Fe_2O_4$ ($x = 0.0$, 0.2, 0.4, 0.6, 0.8 and 1.0) NPs

Samples	H_c (O_e)	M_r (emu/g)	M_s (emu/g)
$CoFe_2O_4$	65.73	11.575	64.85
$Zn_{0.2}Co_{0.8}Fe_2O_4$	36.45	5.5242	45.18
$Zn_{0.4}Co_{0.6}Fe_2O_4$	22.31	1.1323	25.32
$Zn_{0.6}Co_{0.4}Fe_2O_4$	21.74	0.1764	7.125
$Zn_{0.8}Co_{0.2}Fe_2O_4$	6.782	0.0137	3.478
$ZnFe_2O_4$	5.527	0.0016	2.098

3.9 Catalytic Activity

The catalytic oxidation of benzyl alcohol into benzaldehyde was studied by using undoped and Zn^{2+}-doped $CoFe_2O_4$ ($Zn_xCo_{1-x}Fe_2O_4$: $x = 0.0$, 0.2, 0.4, 0.6, 0.8, and 1.0) NPs to investigate their performance as catalysts. In a batch reactor, 0.5 g nanocatalyst ($CoFe_2O_4$, $Zn_{0.2}Co_{0.8}Fe_2O_4$, $Zn_{0.4}Co_{0.6}Fe_2O_4$, $Zn_{0.6}Co_{0.4}Fe_2O_4$, $Zn_{0.8}Co_{0.2}Fe_2O_4$, and $ZnFe_2O_4$) along with the oxidant H_2O_2 (5 mmol) in an

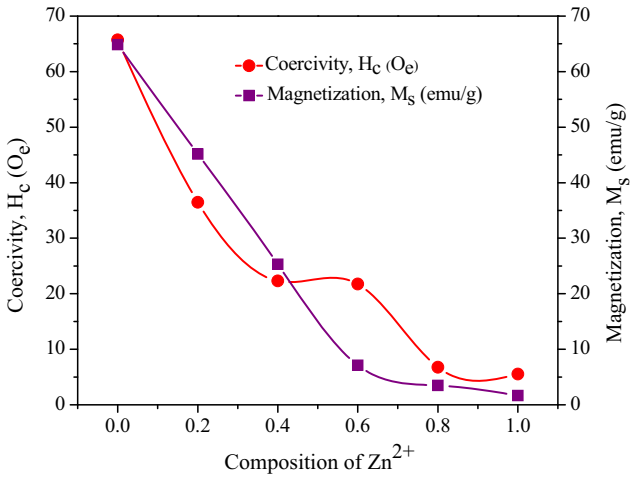

Fig. 12 Variation of the coercivity (H_c) and saturation magnetization (M_s) values of spinel $Zn_xCo_{1-x}Fe_2O_4$ ($x = 0.0$, 0.2, 0.4, 0.6, 0.8, and 1.0) NPs

Table 3 BET surface area, conversion and selectivity of spinel $Zn_xCo_{1-x}Fe_2O_4$ ($x = 0.0$, 0.2, 0.4, 0.6, 0.8 and 1.0) NPs

Samples	BET surface area (m^2/g)	Conversion (%)	Selectivity (%)
$CoFe_2O_4$	58.73	91.73	100
$Zn_{0.2}Co_{0.8}Fe_2O_4$	60.35	93.62	100
$Zn_{0.4}Co_{0.6}Fe_2O_4$	67.48	95.82	100
$Zn_{0.6}Co_{0.4}Fe_2O_4$	63.57	95.07	100
$Zn_{0.8}Co_{0.2}Fe_2O_4$	61.83	94.16	100
$ZnFe_2O_4$	59.17	92.03	100

acetonitrile medium was placed. In order to find competent results for the catalytic oxidation of benzyl alcohol into benzaldehyde, the reaction environments were altered by studying the effect of doping concentration ($x = 0.0$ to 1.0), surface area, and catalyst amount (0.1–0.8 g). The conversion of benzyl alcohol into benzaldehyde reached a maximum of 95.82 % for $Zn_{0.4}Co_{0.6}Fe_2O_4$, whereas for undoped $CoFe_2O_4$, the conversion was 91.73 % with 100 % selectivity (Table 3 and Fig. 13). However, the sample $Zn_{0.4}Co_{0.6}Fe_2O_4$ NPs perform as a good catalyst with higher yield of benzaldehyde with 100 % selectivity than other compositions ($CoFe_2O_4$, $Zn_{0.2}Co_{0.8}Fe_2O_4$, $Zn_{0.6}Co_{0.4}Fe_2O_4$, $Zn_{0.8}Co_{0.2}Fe_2O_4$, and $ZnFe_2O_4$). Hence, the dopant metal (Zn^{2+}) ion is important, which in turn is active for the catalytic oxidation reaction.

The BET surface values of spinel $Zn_xCo_{1-x}Fe_2O_4$ samples are given in Table 3. Undoped spinel $CoFe_2O_4$ NPs possessed a lower surface area of 58.73 m^2/g, whereas it was increased considerably to 67.48 m^2/g for $Zn_{0.4}Co_{0.6}Fe_2O_4$ ($x = 0.4$) and decreased to 59.17 m^2/g ($x = 1.0$), due to the difference in the particle size of the samples, which is also confirmed by XRD, HR-SEM, and HR-TEM results. Therefore, it is believed that the high surface area of spinel $Zn_{0.4}Co_{0.6}Fe_2O_4$ NPs could enhance the catalytic activity than other samples. Usually, catalyst with a high specific surface area would offer more surface active sites and catalytic reaction centers, resulting in the enhancement of catalytic performance. In addition, when the size of particles decreased, the amount of the dispersion of particles per volume in the solution will increase, resulting in the enhancement of the catalytic performance.

The catalytic oxidation of benzyl alcohol into benzaldehyde was found to be increased with increase in the amount of $Zn_{0.4}Co_{0.6}Fe_2O_4$ NPs up to 0.5 g, and further increase in catalyst amount showed negative effect as illustrated in Fig. 14 (Table 4). This may be due to that the increase in the amount of catalyst increased the number of active sites on the surface, which in turn increase the catalytic oxidation of benzyl alcohol into benzaldehyde. When the amount of $Zn_{0.4}Co_{0.6}Fe_2O_4$ NPs increases above the optimum value, the catalytic oxidation is decreased, due to the appearance of turbidity and deposition on the catalyst surface, and hence, the efficiency of the oxidation reduced.

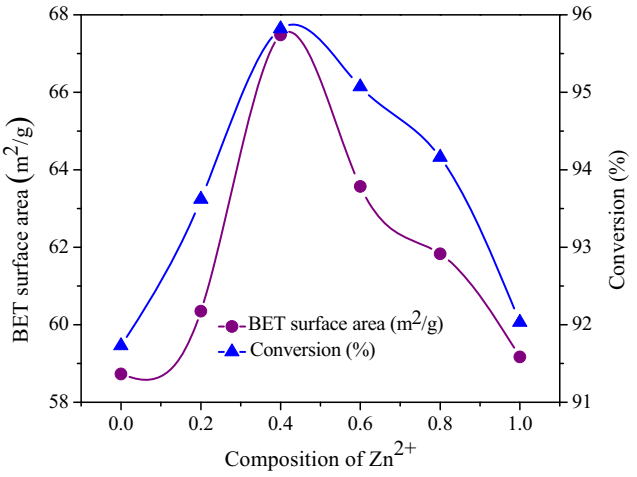

Fig. 13 BET surface area, conversion, and selectivity of spinel $Zn_xCo_{1-x}Fe_2O_4$ ($x = 0.0$, 0.2, 0.4, 0.6, 0.8, and 1.0) NPs (Reaction conditions: Catalysts, 0.5 g; benzyl alcohol, 5 mmol; Acetonitrile, 5 mmol; H_2O_2, 5 mmol; temperature, 80 °C; time, 5 h)

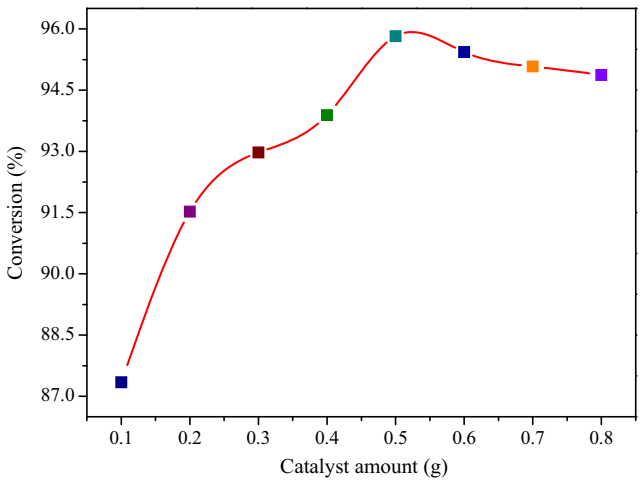

Fig. 14 Effect of the amount of catalyst on the catalytic efficiency (Reaction conditions: Catalysts ($Zn_{0.4}Co_{0.6}Fe_2O_4$), 0.1–0.8 g; benzyl alcohol, 5 mmol; Acetonitrile, 5 mmol; H_2O_2, 5 mmol; temperature, 80 °C; time, 5 h)

Table 4 Amount of catalyst ($Zn_xCo_{1-x}Fe_2O_4$: $x = 0.0$, 0.2, 0.4, 0.6, 0.8 and 1.0) NPs for the catalytic oxidation of benzyl alcohol into benzaldehyde

Catalyst amount (g)	Conversion (%)
0.1	87.34
0.2	91.52
0.3	92.97
0.4	93.88
0.5	95.82
0.6	95.43
0.7	95.18
0.8	95.09

Furthermore, the increase in catalyst concentration beyond the optimum may result in the agglomeration of catalyst particles; hence, the part of the catalyst surface and active catalytic sites becomes unavailable and, thereby, catalytic efficiency decreased. Moreover, a heterogeneous catalyst like Zn-doped $CoFe_2O_4$ spinel is non-toxic, environmentally friendly, and has an excellent catalytic performance. Ramankutty and Sugunan [13] reported $CoFe_2O_4$ is the most active catalyst than other ferrites. Yan et al. [14] reported that the spinel $CoFe_2O_4$ has 93 % selectivity and 63 % conversion of benzyl alcohol into benzaldehyde. Usually, the catalytic oxidation of benzyl alcohol produces a mixture of benzaldehyde, benzoic acid, and benzyl benzoate. However, benzoic acid and benzyl benzoate were not obtained in this present study. Therefore, the catalyst was found to be a highly selective one.

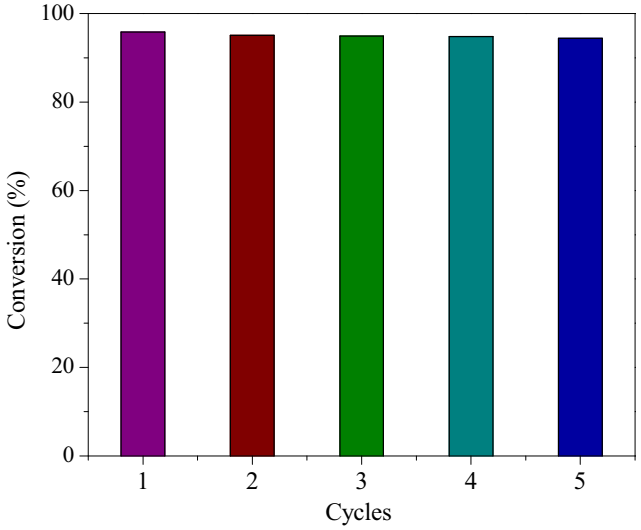

Fig. 15 The reusability of the catalyst for the oxidation of benzyl alcohol to benzaldehyde (Reaction conditions: Catalysts ($Zn_{0.4}Co_{0.6}Fe_2O_4$), 0.5 g; benzyl alcohol, 5 mmol; Acetonitrile, 5 mmol; H_2O_2, 5 mmol; temperature, 80 °C; time, 5 h, Cycles, 5 runs)

The recyclability of nano-catalyst is very important for industrial and technological applications. The reusability of nano-catalyst for the liquid-phase oxidation of benzyl alcohol into benzaldehyde was evaluated, and the results are shown in Fig. 15. The percentage yield versus number of cycles for the reusability of $Zn_{0.4}Co_{0.6}Fe_2O_4$nano-catalyst is shown in Fig. 15. For this purpose, the sample was filtered off from each run and washed several times with ethanol and dried at 110 °C in an air oven for 2 h and was checked for five consecutive runs under the same conditions. During the five runs investigated, the conversion of benzyl alcohol was in a range from 95.82 to 95.09 %, indicating that the catalyst displays good reproducibility and stability. Interestingly, the formation of benzoic acid was not detected. Since the spinel $Mn_{0.6}Zn_{0.4}Fe_2O_4$ nano-catalyst is able to oxidize benzyl alcohol into benzaldehyde with high activity, highly recyclable, remarkably stable, and environmental friendly, they are promising candidates for the industrial applications.

The proposed catalytic mechanism of the spinel $Zn_xCo_{1-x}Fe_2O_4$ nano-catalyzed reaction of acetonitrile-hydrogen peroxide medium is shown in Scheme 1. Initially, solvent acetonitrile can activate the oxidant H_2O_2 forming a perhydroxyl anion (OOH^-), which nucleophilically attacks the nitrile to generate an intermediate peroxycarboximidic acid. It is well known that the formed intermediate is a good oxygen transfer agent. The organic substrate (benzyl alcohol) and the oxidant H_2O_2 dissolve in acetonitrile, which activates H_2O_2 into OOH^- anion and forms Co–OOH^- species [61]. This account revealed that the phenyl ring and the OH group of benzyl alcohol interact with Zn^{2+} ion of $ZnFe_2O_4$ and the inner active sites remain intact. The interaction of phenyl ring and OH group with the outer

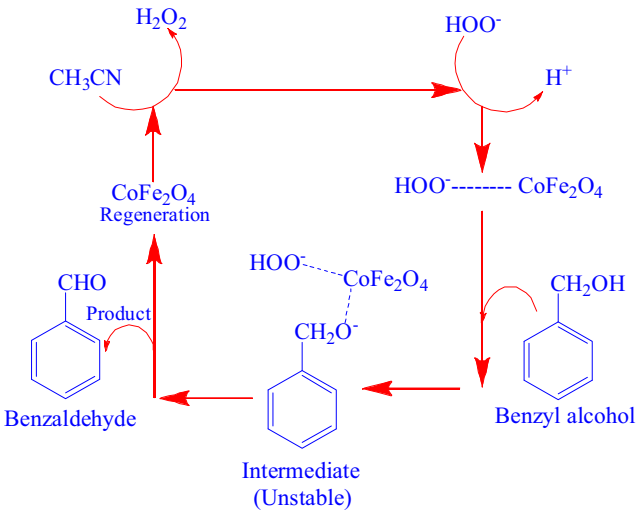

Scheme 1 Schematic diagram of proposed catalytic oxidation pathway of benzyl alcohol into benzaldehyde

metal ions of $CoFe_2O_4$ is also evident by the adsorption of phenyl ring on $CoFe_2O_4$. However, the catalyst surface gets regenerated by the action of the oxidant, which leads to desorption of the product molecules, thereby favoring further oxidation. Hence, this process is of great interest for the selective oxidation of benzyl alcohol into benzaldehyde. It is noted that not only the conversion of benzyl alcohol but also the benzaldehyde selectivity was higher. In addition, H_2O_2 has been proved to be very efficient and environmentally friendly oxidant, since the product is only aldehyde [61].

4 Conclusions

Spinel $Zn_xCo_{1-x}Fe_2O_4$ ($x = 0.0$, 0.2, 0.4, 0.6, 0.8, and 1.0) NPs were successfully synthesized by microwave combustion method using urea as the fuel without using any surfactant and templates. The formation of $Zn_xCo_{1-x}Fe_2O_4$ NPs with pure single-phase cubic structure was confirmed by powder XRD, Rietveld refinement XRD, FT-IR, EDX, and SAED analyses. The average crystallite size of the samples was estimated using the Debye-Scherrer's formula and found to be in the range of 25.43 and 29.46 nm. The lattice parameter is increased from 8.432 to 8.441 Å by increasing the Zn^{2+} content, due to the difference in the ionic radii of Zn^{2+} (0.82 Å) and Co^{2+} (0.72 Å) ions. UV-visible DRS study showed the band gap energy (E_g) of the undoped $CoFe_2O_4$ is 2.69 eV, and by increasing the Zn^{2+} ions, it decreased from 2.61 to 2.01 eV. VSM results for undoped $CoFe_2O_4$ and lower concentration ($x = 0.0$, 0.2 and 0.4) of Zn^{2+}-doped samples showed a ferromagnetic behavior, whereas the higher concentration of Zn^{2+}-doped $CoFe_2O_4$ samples ($x = 0.6$, 0.8 and 1.0) showed a superparamagnetic behavior with hysteresis and that the M_s values decreased with increasing the Zn^{2+} dopant. The catalytic oxidation of benzyl alcohol into benzaldehyde has a conversion of 91.73 % for undoped $CoFe_2O_4$ NPs and 95.82 % for $Zn_{0.4}Co_{0.6}Fe_2O_4$ nanocatalysts. It was observed that the substitution of Zn^{2+} ions in $CoFe_2O_4$ plays a significant role in the alternation and development of crystal structure; morphologies; and optical, magnetic, and catalytic characteristics of the spinel $CoFe_2O_4$ NPs.

References

1. Karaoglu, E., Baykal, A.: J. Supercond. Nov. Magn. **27**, 2041 (2014)
2. Manikandan, A., Durka, M., Arul Antony, S.: J. Supercond. Nov. Magn. **27**, 2841 (2014)
3. Baykal, A., Karaoglu, E., Sozeri, H., Uysal, E., Toprak, M.S.: J. Supercond. Nov. Magn. **26**, 165 (2013)
4. Manikandan, A., Durka, M., Arul Antony, S.: J. Supercond. Nov. Magn. **28**, 209 (2015)
5. Manikandan, A., Hema, E., Durka, M., Seevakan, K., Alagesan, T., Arul Antony, S.: J. Supercond. Nov. Magn. (2015). doi:10.1007/s10948-014-2945-x
6. Zhongli, W., Xiaojuan, L., Minfeng, L., Ping, C., Yao, L., Jian, M.: J. Phys. Chem. B **112**, 11292 (2008)
7. Borgohain, C., Senapati, K.K., Sarma, K.C., Phukan, P.: J. Mol. Catal. A: Chem **363**, 495 (2012)
8. Agrafiotis, C.C., Pagkoura, C., Zygogianni, A., Karagiannakis, G., Kostoglou, M., Konstandopoulos, G.A.: Int. J. Hydrog. Energy **37**, 8964 (2012)
9. Kumbhar, V.S., Jagadale, A.D., Shinde, N.M., Lokhande, C.D.: J. Appl. Surf. Sci **259**, 39 (2012)
10. Kiselev, S.I., Sankey, J.C., Krivorotov, I.N., Emley, N.C., Schoelkopf, R.J., Buhrman, R.A., Ralph, D.C.: Nature **425**, 380 (2003)
11. Borgohain, C., Senapati, K.K., Sarma, K.C., Phukan, P.: J. Mol. Catal. A: Chem **363–364**, 495–500 (2012)
12. Koseoglu, Y., Baykal, A., Toprak, M.S., Gozuak, F., Basaran, A.C., Aktas, B.: J. Alloys Compd. **462**, 209 (2008)
13. Ramankutty, C.G., Sugunan, S.: App. Catal. A: Gen **218**, 39 (2001)
14. Yan, K., Wu, X., An, X., Xie, X.: J. Alloys Compd. **552**, 405 (2013)
15. Koseoglu, Y., Alan, F., Tan, M., Yilgin, R., Ozturk, M.: Ceram. Int. **38**, 3625 (2012)
16. Koseoglu, Y., Baykal, A., Gozuak, F., Kavas, H.: Polyhedron **28**, 2887 (2009)
17. Kasapoglu, N., Baykal, A., Koseoglu, Y., Toprak, M.S.: Scripta Mater **57**, 441 (2007)
18. Manikandan, A., Durka, M., Arul Antony, S.: J. Supercond. Nov. Magn. **28**, 209 (2015)
19. Manikandan, A., Durka, M., Arul Antony, S.: J. Supercond. Nov. Magn. **28**, 1405 (2015)
20. Koseoglu, Y., Alan, F., Tan, M., Yilgin, R., Ozturk, M.: Ceram. Int. **38**, 3625 (2012)
21. Pillai, V., Shah, D.O.: J. Magn. Magn. Mater. **321**, 2170 (2009)
22. Cabuil, V., Dupuis, V., Talbot, D., Naveu, S.: J. Magn. Magn. Mater. **323**, 1238 (2011)
23. Cheng, F., Peng, Z., Liao, C., Xu, Z., Geo, S., Yan, C., Wang, D.: Solid State Commun. **107**, 471 (1998)
24. Sajjia, M., Oubaha, M., Hasanuzzaman, M., Olabi, A.G. Ceram. Int. **40**, 1147 (2014)
25. Zhuang, L., Zhang, W., Zhao, Y., Li, D., Wu, W., Shen, H.: Powder Technol. **217**, 46 (2012)
26. Koseoglu, Y., Oleiwi, M.I.O., Yilgin, R., Kocbay, A.N.: Ceram. Int. **38**, 6671 (2012)
27. Akhtar, M.J., Younas, M.: Solid State Sci. **14**, 1536 (2012)
28. Gao, R.R., Zhang, Y., Yu, W., Xiong, R., Shi, J.: J. Magn. Magn. Mater. **324**, 2534 (2012)
29. Chen, J., Wang, Y., Deng, Y.: J. Alloys Compd. **552**, 65 (2013)
30. Aslibeiki, B., Kameli, P., Salamati, H., Eshraghi, M., Tahmasebi, T.: J. Magn. Magn. Mater. **322**, 2929 (2010)
31. Arora, M., Chauhan, S., Sati, P.C., Kumar, M.: J. Supercond. Nov. Magn. **27**, 1867 (2014)
32. Khan, M.A., Islam, M.U., Ishaque, M., Rahman, I.Z.: J. Alloys Compd. **519**, 156 (2012)
33. Baykal, A., Guner, S., Demir, A.: J. Alloys Compd. **619**, 5 (2015)
34. Cui, L., Guo, P., Zhang, G., Li, Q., Wang, R., Zhou, M., Ran, L., Zhao, X.S.: Colloids Surf. A **423**, 170 (2013)
35. Habibi, M.H., Parhizkar, H.J.: Spectrochim. Acta A **127**, 102 (2014)
36. Gherca, D., Pui, A., Cornei, N., Cojocariu, A., Nica, V., Caltun, O.: J. Magn. Magn. Mater. **324**, 3906 (2012)

37. Rana, S., Philip, J., Raj, B.: Mater. Chem. Phys. **124**, 264 (2010)
38. Azam, A.: J. Alloys Compd. **540**, 145 (2012)
39. Kislova, N., Srinivasan, S.S., Emirov, Y., Stefanakos, E.K.: Mater. Sci. Eng. B **153**, 70 (2008)
40. Ng, C.H.B., Fan, W.Y.: J. Phys. Chem. B **110**, 20801 (2006)
41. Himcinschi, C., Vrejoiu, L., Salvan, G., Fronk, M., Talkenberger, A.: J. Appl. Phys **113**, 1 (2013)
42. Bai, H., Liu, Z., Sun, D.D. Int. J. Hydrog. Energy **37**, 13998 (2012)
43. Ahmed, A.S., Muhamed, S.M., Singk, M.L., Tabassum, S., Naqvi, A.H., Azam, A.: J. Lumin. **131**, 1 (2011)
44. Bhargava, R., Sharma, P.K., Dutta, R.K., Kumar, S., Pandey, A.C., Kumar, N.: Mater. Chem. Phys **120**, 393 (2010)
45. Zang, C.H., Zhang, D.M., Tang, C.J., Fang, S.J., Zong, Z.J., Yang, Y.X., Zhao, C.H., Zhang, Y.S.: J. Phys. Chem. C **113**, 18527 (2009)
46. Zhuge, L.J., Wu, X.M., Wu, Z.F., Yang, X.M., Chen, X.M., Chen, Q.: Mater. Chem. Phys. **120**, 480 (2010)
47. Manikandan, A., Arul Antony, S., Sridhar, R., Bououdina, M.: J. Nanosci. Nanotech. **15**, 4948 (2015)
48. Yilmaz, S., Bacaksiz, E., McGlynn, E., Polat, I., Ozcan, S.: Thin Solid Films **520**, 5172 (2012)
49. Costa, A.C.F.M., Kiminami, R.H.G.A., Santos, P.T.A., Silva, J.F.: J. Mater. Sci. **48**, 172 (2013)
50. Hankare, P.P., Pandav, R.S., Patil, R.P., Vader, V.T., Garadkar, K.M.: J. Alloys Compd. **544**, 197 (2012)
51. Hankare, P.P., Sanadi, K.R., Garadkar, K.M., Patil, D.R., Mulla, I.S.: J. Alloys Compd. **553**, 383 (2013)
52. Koseoglu, Y.: Ceram. Int. **39**, 4221 (2013)
53. Kambale, R.C., Shaikh, P.A., Harale, N.S., Bilur, V.A., Kolekar, Y.D., Bhosale, C.H., Rajpure, K.Y.: J. Alloys Compd. **490**, 568 (2010)
54. Yadav, S.P., Shinde, S.S., Kadam, A.A., Rajpure, K.Y.: J. Alloys Compd. **555**, 330 (2013)
55. Kumar, L., Kumar, P., Kar, M.: J. Alloys. Compd. **551**, 72 (2013)
56. Gherca, D., Pui, A., Cornei, N., Cojocariu, A., Nica, V., Caltun, O.: J. Magn. Magn. Mater. **324**, 3906 (2012)
57. Kurmude, D.V., Kale, C.M., Aghav, P.S., Shengule, D.R., Jadhav, K.M.: J. Supercond. Nov. Magn. **27**, 1889 (2014)
58. Kumar, L., Kumar, P., Srivastava, S.K., Kar, M.: J. Supercond. Nov. Magn. **27**, 1677 (2014)
59. Ati, A.A., Othaman, Z., Samavati, A., Doust, F.Y.: J. Mol. Struct. **1058**, 136 (2014)
60. Gozuak, F., Koseoglu, Y., Baykal, A., Kavas, H. J. Magn. Magn. Mater. **321**, 2170 (2009)
61. Ali, S.R., Chandra, P., Latwal, M., Jain, S.K., Bansal, V.K., Singh, S.P.: Chin. J. Catal. **32**, 1844 (2011)